





Asymmetric guidance of multiple hybrid modes through a gain-loss-assisted planar coupled-waveguide system hosting higher-order exceptional points

Anubhav Paul , Arnab Laha , Sibnath Dey , and Somnath Ghosh *

Unconventional Photonics Laboratory, Department of Physics, Indian Institute of Technology Jodhpur, Rajasthan-342037, India



(Received 21 June 2021; revised 20 November 2021; accepted 22 November 2021; published 6 December 2021)

The gain-loss-assisted optical systems have revealed an unconventional light manipulation tool by hosting exceptional points (EPs), which has lately a great deal of interest in the photonics community. Here, the emergence of higher-order EPs is investigated in a planar coupled-waveguide geometry, which has the potential to assemble additional degrees of freedom to explore EP-induced light dynamics. A planar form of waveguide array consisting of four high-indexed guides is designed to support multiple quasiguided hybrid modes. An inhomogeneous customized gain-loss profile to couple at least three chosen modes is introduced in such a way that the waveguide hosts an EP of order three with the simultaneous presence of two second-order EPs in the gain-loss parameter plane. We investigate the dynamical parametric encirclement schemes of embedded EPs of different orders and exclusively reveal both the chiral and nonchiral dynamics of light assisted by asymmetric conversions of hybrid modes. The implementation of our findings in discrete photonic systems hosting higher-order EPs indeed opens up a fertile platform to meet a wide range of enticing applications in the context of manipulation of modes including conversion and switching.

DOI: [10.1103/PhysRevA.104.063503](https://doi.org/10.1103/PhysRevA.104.063503)

I. INTRODUCTION

Exceptional points (EPs) are a special type of spectral degeneracies that analytically connect the coupled states of usually open or non-Hermitian systems [1,2]. While a system meets an EP, at least two coupled eigenvalues and the corresponding eigenvectors coalesce, simultaneously, and hence, the underlying Hamiltonian becomes defective due to the collapse of eigenspace dimensionality, which refers to an EP as a topological defect [1,3]. A system with at least two-dimensional (2D) tunable parameter space can host multiple second-order EPs (EP2s). Essentially, the order of an EP is decided by the number of coalescing states, i.e., the presence of an EP of order n (say, EP n ; $n \geq 2$) results in the coalescence of n number of coupled states. The realization of such a simultaneous coalescence of n coupled states demands a complex topology of the underlying system associated with $(n^2 + n - 2)/2$ tunable parameters [4–6]. However, the presence of $(n - 1)$ connecting EP2s among n coupled states due to the appropriate customization of only a 2D parameter space can steer alike topological functionalities of an EP n in a comparably simple platform [7–10].

Even though the presence of EPs was thought to be a purely mathematical concept [1] for a long time, over the last two decades, the interplay of gain-loss (non-Hermitian components) with the topology of an optical system has established the branch-point behavior of EPs as a promising tool to control the light states [11–14]. Intense theoretical efforts have lately been put forward to explore the various aspects of the branch-point properties of EPs of different

orders along with associated phases behaviors [15,16] by different matrix formulations [3,17,18]. Moreover, a wide range of fascinating applications, including topologically controlled mode conversion or switching [19–26], unidirectional light propagations [27] with enhanced nonreciprocity [28–30], ultrasensitive detection [31–33], lasing [34,35], and coherent perfect absorption (CPA) [36], topological energy transfer [37], parametric instability to amplify light [38], and so on have been explored by engineering EPs in various gain-loss-assisted optical systems such as waveguides [20,22–26], microresonators [9,33,39], photonic crystals [40,41], lasers [34,35,42], and optomechanical systems [37,43].

A quasistatic variation of coupling parameters enclosing an EP allows permutation among the corresponding coupled states in the sense that the associated eigenvalues adiabatically exchange their initial positions along with the eigenvectors, where one of them acquires an additional Berry's phase [9,44–47]. However, the dynamics of coupled states fail to meet such adiabaticity for dynamical (time-dependent or analogous length-dependent for optical systems) variation of coupling parameters around the respective EP [48,49]. Here, EP-induced nonadiabatic corrections come into the picture to enable chirality with time-asymmetric dynamics of the corresponding coupled states, where due to asymmetric population transfer among them, one of the eigenstates dominates at the end of the encirclement process concerning the direction of parametric variation around the respective EP [48,49]. Lately, the dynamical EP2-encirclement schemes have widely been studied to explore time-asymmetric light dynamics [20,22–26]. Moreover, the nonadiabaticity in light dynamics along with validation or failure of chirality has been reported by implementing dynamical encirclement schemes of multiple connecting EP2s or higher-order EPs in planar or two-

*somiit@rediffmail.com

three-coupled waveguide system [25,26,50]. In this context, the exploration of dynamically encircled higher-order EPs in array-waveguide geometries supporting hybrid modes can potentially unfold additional degrees of freedom in light manipulation toward signal processing and routing. Such studies can be implemented in any of discrete integrated photonic systems to mold the flow of light by using dynamically encircled EP2s or EP3s as tools, however, exclusive analysis and physical insights in this context are lacking.

In this paper, we report a specialty gain-loss-assisted planar coupled-waveguide system to host a pair of connected EP2s in its 2D gain-loss parameter plane, leading to the presence of an EP3 in the same parameter space. Here, the dynamics of multiple quasiguided hybrid modes enabled by different dynamical EP-encirclement schemes are investigated, exclusively. To encounter two connected EP2s, three coupled quasiguided hybrid modes are chosen to study their avoided resonance crossing (ARC) type interactions by introducing a multilayer (customized) unbalanced gain-loss profile based on two tunable parameters. Besides validating the second-order branch-point behavior of the identified EP2s, the effect of individual dynamical encirclement schemes around them is investigated to explore the chiral light dynamics enriched with direction-dependent asymmetric mode conversions among the associated coupled modes. The third-order topological branch-point functionalities of an embedded EP3 among three hybrid modes are established by tailoring a customized parameter space enclosing both the identified EP2s, where the failure of chiral behavior in EP3-induced light dynamics is revealed. The findings indeed open up a versatile platform to explore the unconventional applications of EPs. The physical insights behind such fascinating behaviors of hybrid modes in the vicinity of EPs in a planar coupled-waveguide system can also be explored in optical lattices with long-range correlations.

II. RESULTS AND DISCUSSIONS

A. Configuring a planar coupled-waveguide arrangement

We design a fabrication feasible planar form of a coupled-waveguide arrangement, occupying the regions $-W/2 \leq x \leq W/2$ and $0 \leq z \leq L$ along the transverse (x) and longitudinal (z) directions, respectively, where four equidistant high-indexed (with refractive index n_h) layers, having the width $d = W/11$ of each, are placed over a low-indexed (with refractive index n_l) cladding layer, as shown in Fig. 1(a). We normalize the operating frequency $\omega = 1$ (i.e., the operating wavelength $\lambda = 2\pi$) to implement a dimensionless operation and set the total width $W = 30\lambda/\pi = 60$ and the operating length $L = 20 \times 10^3$ in dimensionless units. The refractive indices are chosen as $n_h = 1.5$ and $n_l = 1.46$ to consider a feasible prototype with the combination of glass- and silica-based materials. The proposed waveguide arrangement supports multiple quasiguided hybrid modes, which are the combination of individual modes guided by the high-indexed layers. To enable the non-Hermitian coupling among the quasiguided modes, a customized gain-loss profile is spatially distributed over the complete waveguide arrangement, where the modal interactions are modulated based on two tunable parameters

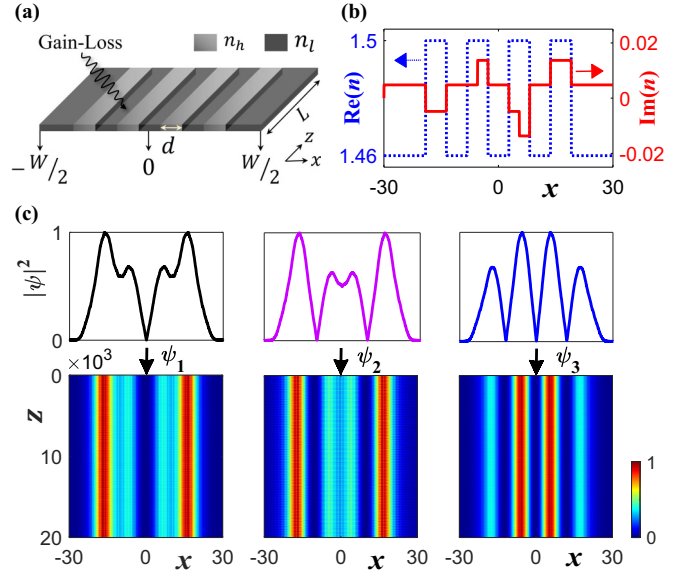


FIG. 1. (a) Schematic diagram of the gain-loss-assisted planar coupled-waveguide arrangement, occupying the regions $-W/2 \leq x \leq W/2$ and $0 \leq z \leq L$ along the transverse (x) and longitudinal (z) directions, respectively. n_h and n_l represent the high and low refractive indices, respectively, where d is the width of each of the high indexed regions. (b) Transverse profile of $n(x)$: Dotted blue line represents the profile of $\text{Re}[n(x)]$ (corresponding to the left vertical axis) and solid red line represents the profile of $\text{Im}[n(x)]$ for a chosen $\gamma = 0.0048$ and $\tau = 2.8515$ (corresponding to the right vertical axis). (c) Normalized field-intensities of three chosen quasiguided modes ψ_j ($j = 1, 2, 3$) (top panel) and their propagations (bottom panel) through the passive (without any gain-loss) waveguide system.

associated with the gain-loss profile viz. gain-loss coefficient (γ) and a loss-to-gain ratio (τ). The overall transverse profile of complex refractive index distribution can be written as

$$n(x) = \begin{cases} n_l + i\gamma, & \text{for } \begin{cases} 7W/22 \leq |x| \leq W/2 \\ 3W/22 \leq |x| \leq 5W/22 \\ -W/22 \leq x \leq W/22 \end{cases} \\ n_h - i\gamma, & \text{for } \begin{cases} -7W/22 \leq x \leq -5W/22 \\ W/22 \leq x \leq W/11 \end{cases} \\ n_h + i\gamma, & \text{for } -3W/22 \leq x \leq -W/11 \\ n_h + i\tau\gamma, & \text{for } \begin{cases} -W/11 \leq x \leq -W/22 \\ 5W/22 \leq x \leq 7W/22 \end{cases} \\ n_h - i\tau\gamma, & \text{for } W/11 \leq x \leq 3W/22 \end{cases} \quad (1)$$

The complex refractive index profile for a specific transverse cross section (i.e., for a chosen γ and τ) is shown in Fig. 1(b). Physically, τ defines the system's openness based on the coefficient γ . A fixed $\tau = 1$ leads to the system's operation in a particular \mathcal{PT} phase; however, we consider τ as a variable (beyond \mathcal{PT} symmetry) to modulate $\text{Im}(n)$ associated with an unbalanced gain-loss profile toward emergence of an EP3 with the simultaneous presence of two connected EP2s. The proposed coupled waveguide geometry offers a further scope of scalability, where associated feasible prototypes can be realized by state-of-the-art thin-film deposition technology with

a combination of glass and silica-glass-based materials, where the patterned attenuation and gain can be achieved straightforwardly by controlled doping of lossy and active materials using a standard photolithography technique.

To investigate the emergence of an EP3 with a pair of two connecting EP2s, we choose three quasiguided hybrid modes ψ_j ($j = 1, 2, 3$) and study their interactions based on the variation of corresponding propagation constants β_j ($j = 1, 2, 3$) over the tunability of the control parameters γ and τ . Here, the scalar modal equation (owing to small Δn approximation; $\Delta n = n_h - n_l$)

$$[\partial_x^2 + n^2(x)\omega^2 - \beta^2]\psi(x) = 0 \quad (2)$$

associated with $n(x)$ given in Eq. (1) is solved to compute the β values of the chosen modes. Without onset of any gain-loss profile, the normalized field intensities of ψ_j ($j = 1, 2, 3$) are shown in the top panel of Fig. 1(c), where in the bottom panel, the propagation of them through the passive system are displayed.

B. Hosting of two connecting EP2s and an EP3

The chosen hybrid modes ψ_j ($j = 1, 2, 3$) are mutually coupled with the onset of non-Hermiticity in terms of the customized gain-loss profile. We tune the control parameters γ and τ judiciously to encounter a pair of connecting EP2s among ψ_j ($j = 1, 2, 3$) for different judiciously chosen τ values [9]. Such ARC-type interactions among β_j with crossing or anticrossing of $\text{Re}(\beta)$ and $\text{Im}(\beta)$ are shown in Fig. 2.

In Fig. 2(a), a strong interaction between β_1 and β_2 concerning an increasing variation of γ is shown, where β_3 behaves as an observer. For a specifically chosen $\tau = 1.8$, β_1 and β_2 exhibit an ARC within $0.0018 \leq \gamma \leq 0.003$, where $\text{Re}(\beta)$ goes through an anticrossing and $\text{Im}(\beta)$ experiences a simultaneous crossing, as shown in the top panel of Fig. 2(a.1). However, for a slightly higher $\tau = 1.9$, a different topology of the ARC between β_1 and β_2 for the same γ range can be observed in the bottom panel of Fig. 2(a.1), where $\text{Re}(\beta)$ experiences a crossing with a simultaneous anticrossing in $\text{Im}(\beta)$. Such two topologically dissimilar ARCs between β_1 and β_2 refer to the presence of a topological branch point, i.e., an EP2 for an intermediate τ . Hence, we judiciously choose $\tau = 1.8625$ and track the trajectories of β_j in Fig. 2(a.2), where β_1 and β_2 coalesce at $\gamma \approx 0.0023$ and lose their identities, however, β_3 moves as an observer. Thus, we encounter an EP2 between ψ_1 and ψ_2 , say EP2^(1,2), at $\{\gamma = 0.0023, \tau = 1.8625\}$.

Similarly, in Fig. 2(b), we show the encounter of an EP2, say EP2^(2,3), to connect β_2 and β_3 analytically. With judicious tuning of the coupling parameters, we observe that β_2 and β_3 interact strongly within $0.011 \leq \gamma \leq 0.014$, where β_1 behaves as an observer. As can be seen in the top panel of Fig. 2(b.1), β_2 and β_3 exhibit ARC, concerning an increasing γ , with a simultaneous anticrossing and crossing of their $\text{Re}(\beta)$ and $\text{Im}(\beta)$, respectively, for a chosen $\tau = 1.35$. In contrast, for $\tau = 1.45$, a topologically different ARC between β_2 and β_3 can be observed in the bottom panel of Fig. 2(b.1) for the same variation of γ , where $\text{Re}(\beta)$ and $\text{Im}(\beta)$ simulta-

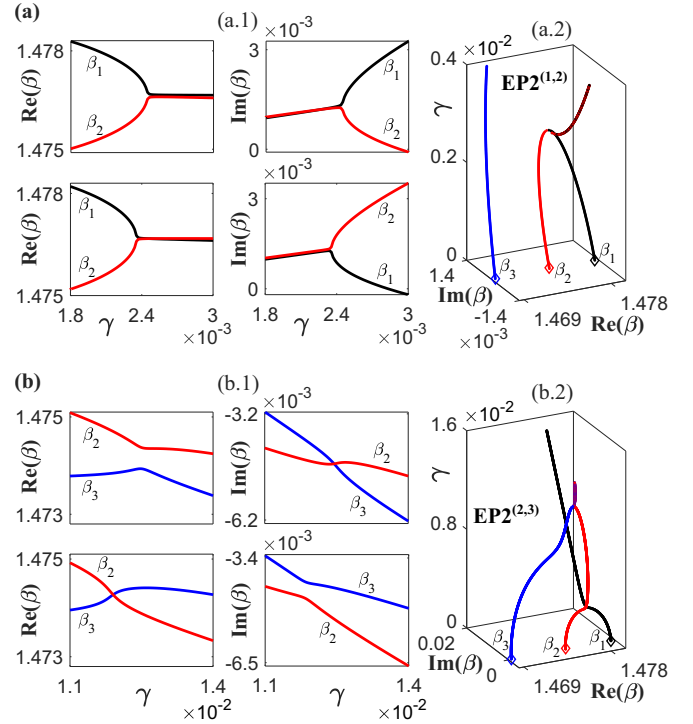


FIG. 2. (a): (a.1) Trajectories of β_1 (dotted black curve) and β_2 (dotted red curve) exhibiting an ARC within the γ range $0.0018 \leq \gamma \leq 0.003$ with a simultaneous anticrossing and crossing in $\text{Re}(\beta)$ and $\text{Im}(\beta)$, respectively, for a chosen $\tau = 1.8$ (top panel), and a topologically different ARC within the same γ range with a simultaneous crossing and anticrossing in $\text{Re}(\beta)$ and $\text{Im}(\beta)$, respectively, for a slightly higher $\tau = 1.9$ (bottom panel). (a.2) Trajectories of β_1 , β_2 , and β_3 (dotted blue curve) for a chosen intermediate value of $\tau = 1.8625$, where β_1 and β_2 coalesce at $\gamma \approx 0.0023$ referring to the presence of EP2^(1,2) at $\sim(0.0023, 1.8625)$ in the (γ, τ) -plane, and β_3 moves unaffectedly concerning the increasing variation of γ . (b): (b.1) Trajectories of β_2 and β_3 exhibiting an ARC within the γ range $0.011 \leq \gamma \leq 0.014$ with a simultaneous anticrossing and crossing in $\text{Re}(\beta)$ and $\text{Im}(\beta)$, respectively, for a chosen $\tau = 1.35$ (top panel), and a topologically different ARC within the same γ range with a simultaneous crossing and anticrossing in $\text{Re}(\beta)$ and $\text{Im}(\beta)$, respectively, for a slightly higher $\tau = 1.45$ (bottom panel). (b.2) Trajectories of β_1 , β_2 , and β_3 for a chosen intermediate value of $\tau = 1.4225$, where β_2 and β_3 coalesce at $\gamma \approx 0.0122$ referring to the presence of EP2^(2,3) at $\sim(0.0122, 1.4225)$ in the (γ, τ) plane, and β_1 moves unaffectedly concerning the increasing variation of γ . The trajectories of β_3 in (a.1) and β_1 in (b.1) are not shown to emphasize the respective crossing and anticrossing phenomena. The diamond markers of respective colors in (a.2) and (b.2) indicate the initial positions (i.e., for $\gamma = 0$) of β_j .

neously experience crossing and anticrossing, respectively. In Fig. 2(b.2), we show the trajectories of β_j , while choosing an intermediate $\tau = 1.4225$. Here, β_2 and β_3 coalesce (unaffectedly β_1) at $\gamma \approx 0.0122$, referring to the presence of EP2^(2,3) in the (γ, τ) plane at $\sim(0.0122, 1.4225)$.

Thus, we encounter two connecting EP2s among three coupled hybrid modes ψ_j ($j = 1, 2, 3$) by varying only two coupling parameters γ and τ . Here, we can observe two such situations that when two of three chosen modes interact

strongly in the vicinity of a second-order branch point, then the third mode behaves as an observer. This is the exclusive signature of the presence of a third-order branch point, i.e., an EP3 within the chosen interaction regime of the same parameter space, where all the three chosen modes are analytically connected [8,9].

C. Quasistatic parametric encirclement schemes around the identified EPs

Here, we examine the second- and third-order branch-point features of the identified EP2s by considering three different parametric encirclement schemes in the (γ, τ) plane governed by the equation:

$$\gamma(\alpha) = \gamma_0 \sin\left(\frac{\alpha}{2}\right) \quad \text{and} \quad \tau(\alpha) = \tau_0 + p \sin(\alpha). \quad (3)$$

Equation (3) can lead to the simultaneous variation of the control parameters γ and τ along a closed elliptically shaped loop around single or both the identified EP2s based on the appropriate choices of characteristics parameter γ_0 (should be greater than the γ value of the respective EP2 to be encircled), τ_0 and p over the tunable angle α ($0 \leq \alpha \leq 2\pi$, where $\alpha : 0 \rightarrow 2\pi$ leads the clockwise variation and $\alpha : 2\pi \rightarrow 0$ leads the anticlockwise variation for $p > 0$). Such a specific shape of parameter space is chosen to consider $\gamma = 0$ at both the beginning and the end of the encirclement process. Figure 3(a) shows such three loops in the (γ, τ) plane. Here, Loop 1 (described by the parameters $\gamma_0 = 0.003$, $\tau_0 = 1.8625$ and $p = 0.3$) and Loop 2 (described by the parameters $\gamma_0 = 0.014$, $\tau_0 = 1.4225$, and $p = 0.6$) individually encircle EP2^(1,2) and EP2^(2,3), respectively, whereas Loop 3 described by the parameters $\gamma_0 = 0.014$, $\tau_0 = 1.8625$, and $p = 0.6$ encircles both EP2^(1,2) and EP2^(2,3) simultaneously. In Figs. 3(b)–(d), we display the trajectories of β_j ($j = 1, 2, 3$) (propagation constants of the coupled hybrid modes) following the quasistatic variation of γ and τ in the clockwise direction along these three loops, respectively.

We show in Fig. 3(b) that following the quasistatic parametric variation along Loop 1 that encloses only EP2^(1,2) (keeping EP2^(2,3) at outside) in the (γ, τ) plane, the β values of corresponding analytically connected hybrid modes, i.e., β_1 and β_2 are adiabatically permuting locations in the complex β plane and completely exchange their initial positions with the completion of the encirclement process. Here, β_3 remains unaffected from the interaction of β_1 and β_2 due to the encirclement process along Loop 1 and makes an individual loop (avoiding any permutation) in the complex β plane. Here, β_1 and β_2 regain their initial positions upon completing the second-round parametric encirclement process, which reveals the second-order branch point behavior of EP2^(1,2). Similarly, the second-order branch point behavior of EP2^(2,3) can be established from the trajectories of complex β_j shown in Fig. 3(c), while considering the quasistatic parametric encirclement process along Loop 2, which encircles only EP2^(2,3) (keeping EP2^(1,2) at outside). Here, for one complete cycle in the (γ, τ) plane, β_2 and β_3 , which are analytically connected through EP2^(2,3), adiabatically flip their initial positions in the complex β plane, however, β_1 remains unaffected from the overall interaction of β_2 and β_3 and makes an individual loop.

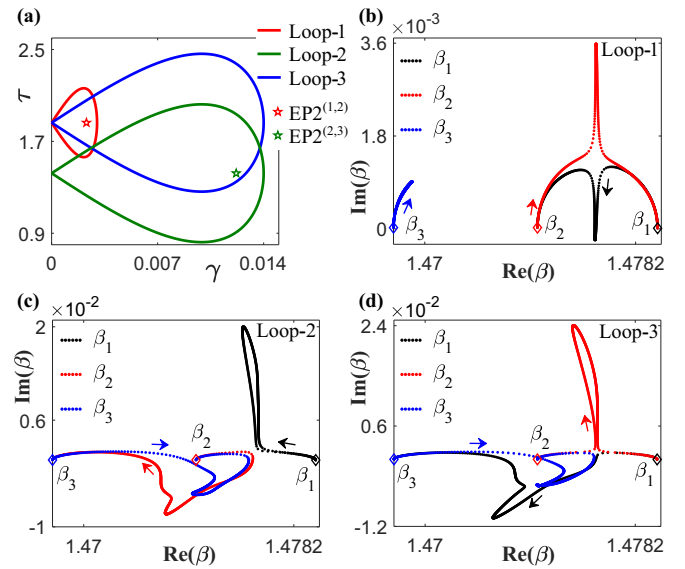


FIG. 3. (a) Chosen parametric loops in the (γ, τ) plane following Eq. (3): Loop 1 (red contour) and Loop 2 (green contour) individually encircle EP2^(1,2) (red star) and EP2^(2,3) (green star), respectively, whereas Loop 3 (blue contour) encircles both EP2^(1,2) and EP2^(2,3) simultaneously. Trajectories of β_1 (dotted black curve), β_2 (dotted red curve), and β_3 (dotted blue curve) in the complex β plane following a clockwise quasistatic variation of γ and τ along (b) Loop 1, displaying an adiabatic exchange process $\beta_1 \rightarrow \beta_2 \rightarrow \beta_1$ unaffected $\beta_3 \rightarrow \beta_3$; (c) Loop 2, exhibiting an adiabatic exchange process $\beta_2 \rightarrow \beta_3 \rightarrow \beta_2$ unaffected $\beta_1 \rightarrow \beta_1$; (d) Loop 3, showing a successive adiabatic exchange process $\beta_1 \rightarrow \beta_3 \rightarrow \beta_2 \rightarrow \beta_1$. In (b)–(d), point-to-point evolution along a particular parametric loop precisely governs the point-to-point progressions in the trajectories of complex β values. The diamond markers of respective colors indicate the initial positions of β_j , where the arrows of respective colors refer to their directions of progression.

It is evident that β_2 and β_3 can regain their initial states for the second parametric cycle along Loop 2. Thus from the trajectories of complex β_j ($j = 1, 2, 3$) following the parametric encirclement process along Loop 1 ($\beta_1 \rightarrow \beta_2 \rightarrow \beta_1$; $\beta_3 \rightarrow \beta_3$) and Loop 2 ($\beta_1 \rightarrow \beta_1$; $\beta_2 \rightarrow \beta_3 \rightarrow \beta_2$), as shown in Figs. 3(b) and 3(c), we reveal the second-order branch point features of two connecting EP2s associated with three coupled hybrid modes ψ_j ($j = 1, 2, 3$).

In Fig. 3(d), we plot the trajectories of β_j ($j = 1, 2, 3$), while varying γ and τ quasistatically in the clockwise direction along Loop 3, which encircles both EP2^(1,2) and EP2^(2,3) simultaneously. Here, the encirclement process along Loop 3 drives a permutation among the propagation constants of all the three coupled hybrid modes, as can be seen in Fig. 3(d), where we have observed that β_1 , β_2 , and β_3 adiabatically exchange their initial positions following a successive manner $\beta_1 \rightarrow \beta_3 \rightarrow \beta_2 \rightarrow \beta_1$ in the complex β plane. We also observe that the β values adiabatically exchange their identities in a reverse sequence, i.e., $\beta_1 \rightarrow \beta_2 \rightarrow \beta_3 \rightarrow \beta_1$, for the anticlockwise encirclement scheme along Loop 3. Here, three successive parametric cycles enclosing both the connecting EP2s are required to regain their initial positions. Such interactions among ψ_j ($j = 1, 2, 3$) due to an encirclement

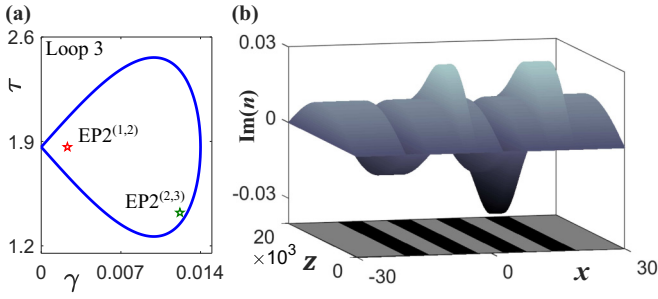


FIG. 4. (a) Loop 3 to encircle both $EP2^{(1,2)}$ and $EP2^{(2,3)}$, respectively, [same Loop 3 as already been shown in Fig. 3(a)]. (b) Overall distribution of $\text{Im}[n(x, z)]$ after mapping Loop 3 [following Eq. (4)] throughout the operating length of the waveguide. The color variation in the ground surface schematically describes the distribution of $\text{Re}[n(x, z)]$, the black and gray colors refer the refractive indices n_h and n_l , respectively.

process enclosing their two connecting EP2s establishes the third-order branch point feature, revealing the appearance of an embedded EP3.

D. Dynamical parametric encirclement scheme around the identified EPs

Here, we study the actual propagation of the quasiguided hybrid modes ψ_j ($j = 1, 2, 3$) following the dynamical parametric variations along the chosen loops shown in Fig. 3(a). Now, to realize a dynamical encirclement scheme along any of the parametric loops, we have to map the corresponding gain-loss variation [i.e., essentially the $\text{Im}(n)$] along the propagation direction of the waveguide system so that one complete parametric cycle along any particular loop is equivalent to one complete pass of light through the length of the waveguide. Such a parameter space mapping can be realized by replacing α in Eq. (3) with $(2\pi z/L)$ (i.e., for $z = 0$ and L , $\alpha = 0$ and 2π , respectively), where the length dependent parameter space can be written as

$$\gamma(\alpha) = \gamma_0 \sin\left(\frac{\pi z}{L}\right) \quad \text{and} \quad \tau(\alpha) = \tau_0 + p \sin\left(\frac{2\pi z}{L}\right). \quad (4)$$

Here clockwise dynamical encirclement scheme ($\alpha : 0 \rightarrow 2\pi$) can be realized by exciting the light modes at $z = 0$ (i.e., considering the propagation from $z = 0$ to $z = L$), whereas the anticlockwise dynamical encirclement scheme ($\alpha : 2\pi \rightarrow 0$) can be realized by exciting the light modes at $z = L$ (i.e., considering the propagation from $z = L$ to $z = 0$). In Fig. 4, the mapping of parameter space governed by Loop 3 [as shown in Fig. 4(a); the same Loop 3 as shown in Fig. 3(a)] is shown by following Eq. (4), where Fig. 4(b) displays the corresponding overall gain-loss distribution in terms of $\text{Im}[n(x, z)]$. For proper understanding, the distribution of $\text{Re}[n(x, z)]$ is depicted schematically by the color variation in the ground surface of Fig. 4(b). In this context, the role of starting or end point of the EP-encirclement process was investigated to understand the chiral aspect (direction dependence) of the light dynamics, where chiral or nonchiral light dynamics were achieved based on the \mathcal{PT} phase of different starting-point [23,25]. However, procurement of passive modes at both input and output is ideal for any device application, that can be

carried out by mapping $\gamma = 0$ at both the ports [using Eq. (3) and Eq. (4)].

The propagation of hybrid modes governed by a dynamical EP-encirclement scheme follows the time-dependent Schrödinger equation (TDSE), which can be realized in terms of 2D scalar beam propagation equation (as z axis plays the role of t axis for photonic systems) under the paraxial approximation as

$$\left[\partial_x^2 + \Delta n^2(x, z)\omega^2\right]\psi(x, z) = -2i\omega\partial_z\psi(x, z) \quad (5)$$

with $\Delta n^2(x, z) \equiv n^2(x, z) - n_l^2$. We exploit the split-step Fourier method to solve the scalar beam propagation equation.

In Fig. 5, we analyze the propagation of chosen hybrid modes ψ_j ($j = 1, 2, 3$), while dynamically encircling each of the encountered EP2s individually. The dynamics of ψ_1 and ψ_2 following the dynamical parametric variations along Loop 1 that encircles only $EP2^{(1,2)}$ (keeping $EP2^{(2,3)}$ outside) are shown in Fig. 5(a). As can be seen in Fig. 5(a.1), during the encirclement in the clockwise direction, both the hybrid modes ψ_1 and ψ_2 at $z = 0$ are converted to ψ_2 at $z = L$, which is beyond the adiabatic exchange between β_1 and β_2 shown in Fig. 3(b). Here, ψ_1 follows the adiabatic expectations and converted to ψ_2 , whereas ψ_2 experiences a nonadiabatic transition and remains in ψ_2 . On the other hand, while implementing the dynamical encirclement scheme in the anticlockwise direction along Loop 1, we observe that both ψ_1 and ψ_2 excited from $z = L$ are converted to ψ_1 at $z = 0$, as shown in Fig. 5(a.2). In this case, nonadiabatic transition of ψ_1 and adiabatic transition of ψ_2 are evident. Thus, depending on the direction of propagation, we observe chiral dynamics of ψ_1 and ψ_2 enriched with an asymmetric mode conversion process, where the conversions $\{\psi_1, \psi_2\} \rightarrow \psi_2$ are observed during the propagation from $z = 0$ to $z = L$ and the conversions $\{\psi_1, \psi_2\} \rightarrow \psi_1$ are observed during the propagation in the opposite direction. The normalized field intensities at both the input and output are shown for each of the beam propagation plots.

In a similar way, we show the chirality-driven asymmetric mode conversion process between ψ_2 and ψ_3 in Fig. 5(b), while implementing the dynamical encirclement scheme along Loop 2 that encloses only $EP2^{(2,3)}$. Here, during the propagation from $z = 0$ to $z = L$ (i.e., for clockwise encirclement), the proposed device allows the conversion $\{\psi_2, \psi_3\} \rightarrow \psi_2$ with adiabatic transition of ψ_3 and nonadiabatic transition of ψ_2 , as shown in Fig. 5(b.1). On the other hand, during the propagation from $z = L$ to $z = 0$ (i.e., for anticlockwise encirclement), the conversions $\{\psi_2, \psi_3\} \rightarrow \psi_3$ with adiabatic transition of ψ_2 and nonadiabatic transition of ψ_3 can be observed in Fig. 5(b.2).

During the implementation of dynamical encirclement schemes, the adiabaticity in modal dynamics fails (despite valid during the quasistatic encirclement schemes with length-independent parametric variation) due to the relative-gain factors among the interacting modes [48]. The relative-gain terms, appearing in the associated nonadiabatic correction factors, play the key role in such asymmetric modal dynamics, where only the mode that evolves with lower average loss transits adiabatically. The average loss during the evolution of a particular mode can be estimated as $\oint \text{Im}(\beta)/2\pi$ with $\text{Im}(\beta)$ associated with the trajectories of corresponding

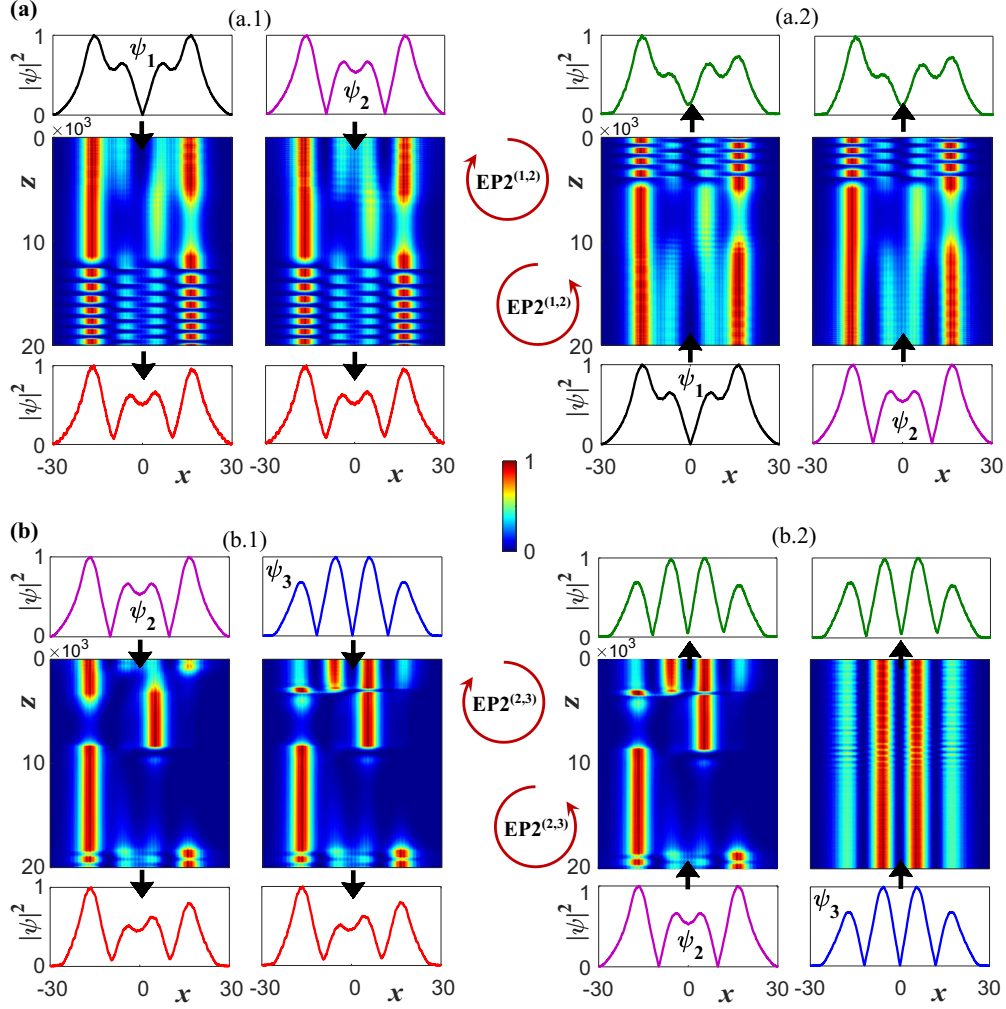


FIG. 5. (a) Propagation of ψ_1 and ψ_2 following the dynamical gain-loss variation along Loop 1 [that encircles $\text{EP2}^{(1,2)}$] in (a.1) the clockwise direction (from $z = 0$ to $z = L$), exhibiting the asymmetric conversions $\{\psi_1, \psi_2\} \rightarrow \psi_2$; (a.2) the anticlockwise direction (from $z = L$ to $z = 0$), exhibiting the asymmetric conversions $\{\psi_1, \psi_2\} \rightarrow \psi_1$. (b) Propagation of ψ_2 and ψ_3 following the dynamical gain-loss variation along Loop 2 [that encircles $\text{EP2}^{(2,3)}$] in (b.1) the clockwise direction (from $z = 0$ to $z = L$), exhibiting the asymmetric conversions $\{\psi_2, \psi_3\} \rightarrow \psi_2$; (b.2) the anticlockwise direction (from $z = L$ to $z = 0$), exhibiting the asymmetric conversions $\{\psi_2, \psi_3\} \rightarrow \psi_3$. During the computation, the field intensities are renormalized after each step evolution for clear visualization of the mode profiles throughout their propagations. The normalized field intensities at both the input and output are shown for each of the beam propagation plots [black, violet, and blue curves represent the field intensities of ψ_1 , ψ_2 , and ψ_3 (respectively) at inputs, whereas the red and green curves represent the outputs for clockwise and anticlockwise encirclements, respectively, for each cases].

β value during the encirclement process. While considering the encirclement along Loop 1, we observe that β_1 evolves with a lower average for the clockwise direction, whereas β_2 evolves with a lower average for the anticlockwise direction. Accordingly, we can see the adiabatic conversion of $\psi_1 (\rightarrow \psi_2)$ and nonadiabatic evolution of $\psi_2 (\rightarrow \psi_2)$ in Fig. 5(a.1), whereas the nonadiabatic evolution of $\psi_1 (\rightarrow \psi_1)$ and adiabatic conversion of $\psi_2 (\rightarrow \psi_1)$ in Fig. 5(a.2). In a similar way, the adiabatic and nonadiabatic transitions for the beam propagation results shown in Fig. 5(b) can be understood by calculating the average losses encountered by β_2 and β_3 during the evolutions along Loop 2 in both the clockwise and the anticlockwise directions (separately). Thus, owing to the breakdown of adiabaticity in modal dynamics induced by the relative-gain factors during the individual dynamical encirclements of each of the EP2s, the proposed device hosts

the chiral property and allows direction-dependent asymmetric mode conversion between the corresponding hybrid modes.

We also calculate the conversion efficiencies in terms of overlap integrals [19] between the fields at input (ψ_i) and output (ψ_o) as

$$C_{i \rightarrow o} = \frac{\left| \int \psi_i \psi_o dx \right|^2}{\int |\psi_i|^2 dx \int |\psi_o|^2 dx}, \quad \{i, o\} \in \{1, 2, 3\} \quad (6)$$

for all the beam propagation plots shown in Fig. 5. The measurement of conversion efficiencies gives a more appropriate insight to understand the transmission of hybrid modes along with associated asymmetric conversions. $C_{i \rightarrow o}$

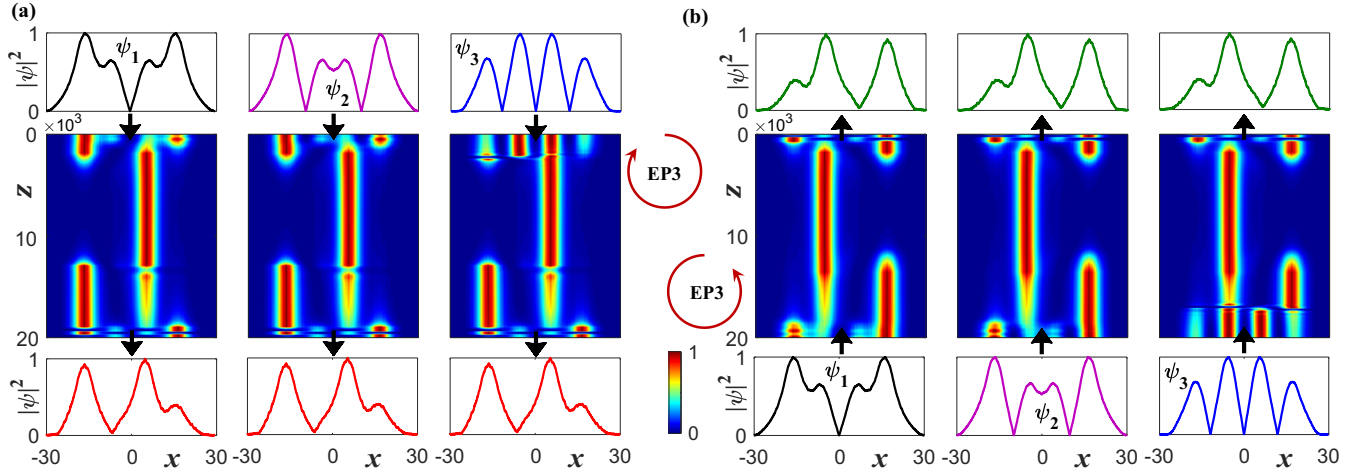


FIG. 6. Propagation of ψ_j ($j = 1, 2, 3$), following the dynamical gain-loss variation governed by Loop 3 (as shown in Fig. 4), which encloses the embedded EP3 with the simultaneous presence of two connected EP2s: (a) and (b) represent the beam propagation results for dynamical encirclement in the clockwise and anticlockwise direction, respectively, where for both the cases ψ_1 dominates at the output following the conversions $\{\psi_1, \psi_2, \psi_3\} \rightarrow \psi_1$. During the computation, the field-intensities are renormalized after each step evolution for clear visualization of the mode profiles throughout their propagations. The normalized field intensities at both the input and output are shown for each of the beam propagation plots [black, violet, and blue curves represent the field intensities of ψ_1 , ψ_2 , and ψ_3 (respectively) at inputs, whereas the red and green curves represent the outputs for clockwise and anticlockwise encirclements, respectively, for each cases].

represents the efficiency for the conversion $\psi_i \rightarrow \psi_o$. Here, along with the choice of gain-loss parameter space, the effective length of the device has been optimized to obtain maximum conversion efficiencies. While encircling EP2^(1,2) individually along Loop 1, we find maximum conversion efficiencies of 95.8% (average) for the conversions $\{\psi_1, \psi_2\} \rightarrow \psi_2$ and 91% (average) for the conversions $\{\psi_1, \psi_2\} \rightarrow \psi_1$. On the other hand, while encircling EP2^(2,3) individually along Loop 2, maximum conversion efficiencies of 94.2% (average) for the conversions $\{\psi_2, \psi_3\} \rightarrow \psi_2$ and 97% (average) for the conversions $\{\psi_2, \psi_3\} \rightarrow \psi_3$ are obtained.

Moreover, to implement the dynamical parametric encirclement scheme around an embedded EP3 with the simultaneous presence of two connecting EP2s, the gain-loss parameter space governed by Loop 3, that encircles both EP2^(1,2) and EP2^(2,3), is mapped throughout the operating length of the waveguide, as already been shown in Fig. 4. The propagation of hybrid modes ψ_j ($j = 1, 2, 3$) following such a dynamical encirclement process are shown in Fig. 6. In Fig. 6(a), we show the beam propagation results for the parametric variation in the clockwise direction, where during the propagation of light from $z = 0$ to $z = L$, it can be observed that all the three hybrid modes are collapsed to ψ_1 , i.e., $\{\psi_1, \psi_2, \psi_3\} \rightarrow \psi_1$, beyond the adiabatic expectations followed by the associated β values as shown in Fig. 3(d). Here, only ψ_2 follows the adiabatic conversion, whereas, ψ_1 and ψ_3 evolves nonadiabatically. In Fig. 6(b), the propagations of ψ_j ($j = 1, 2, 3$) are shown, while implementing the anticlockwise encirclement scheme along Loop 3. Here, we observe that all the three hybrid modes propagating from $z = L$ to $z = 0$ are collapsed to ψ_1 , similar to the case for clockwise encirclement scheme. However, in this case, ψ_3 evolves adiabatically, whereas, ψ_1 and ψ_2 follow nonadiabatic transitions. From the overlap of field intensities at both the input and output, a maximum of 85.8% (average) conversion efficiency

has been obtained for the conversions $\{\psi_1, \psi_2, \psi_3\} \rightarrow \psi_1$ (in both directions).

During the dynamical encirclement of the embedded EP3, the adiabatic and nonadiabatic transitions for encirclement in both the directions can also be verified by calculating the average loss experienced by the hybrid modes during propagations, where we observe that ψ_2 evolves with a lower average loss in the forward direction ($z = 0$ to L) and follows the adiabatic conversion $\psi_2 \rightarrow \psi_1$ (as per the adiabatic expectation $\beta_2 \rightarrow \beta_1$ in the associated sequence $\beta_1 \rightarrow \beta_3 \rightarrow \beta_2 \rightarrow \beta_1$), whereas ψ_3 evolves with a lower average loss in the backward direction ($z = L$ to 0) and follows the adiabatic conversion $\psi_3 \rightarrow \psi_1$ (as per the adiabatic expectation $\beta_3 \rightarrow \beta_1$ in the associated sequence $\beta_1 \rightarrow \beta_2 \rightarrow \beta_3 \rightarrow \beta_1$). Thus, irrespective of the direction of propagation, the proposed device delivers a particular dominating output mode, which refers to the nonchiral property of the device while operating around an EP3 with two connected EP2s.

III. CONCLUSION

In summary, we report the hosting of second- and third-order EPs in an open planar coupled-waveguide arrangement supporting multiple quasiguided hybrid modes. Two connecting EP2s are encountered among three chosen hybrid modes by modulating the ARC-type interactions based on the tunability of two coupling control parameters associated with the gain-loss profile. Here, a customized gain-loss parameter space enclosing both the identified EP2s has driven the topological branch-point functionalities of an embedded EP3 in terms of successive switching among the propagation constants of the corresponding hybrid modes. Dynamically encircling two connecting EP2s individually in the parameter space, we establish the chiral property of the device in terms of direction-dependent asymmetric mode process between two corresponding modes even in the presence of a

third mode. Moreover, the breakdown of such chiral property is established by considering the dynamic variation of coupling parameters around the embedded EP3 with the simultaneous presence of two connecting EP2s, where all the modes are collapsed in a particular dominating mode, regardless of the direction of light propagation. We exclusively explore the properties of hybrid modes around higher-order EPs in a coupled planar waveguide structure, where the design methodology along with the mechanisms of encounter and dynamical encirclement of different orders of EPs can be implemented in any discrete integrated photonic system for the manipulation of light modes. The proposed platform enriched with EP-induced mode conversion or switching schemes and the associated design methodology indeed facilitate the growth of high-performance integrated and on-chip photonic circuits for signal processing and routing in future optical communication systems.

ACKNOWLEDGMENT

A.L. and S.G. acknowledge the financial support from the Science and Engineering research Board (SERB) (Grant No. ECR/2017/000491), Department of Science and Technology, Government of India.

APPENDIX

We also plot the profiles of $|\psi|^2$ at different z associated with the beam propagation plots shown in Fig. 5 and 6. Figure 7 shows such four beam evolution plots to exemplify beam evolution phenomena for different dynamical encirclement schemes. Figures 7(a.1) and 7(a.2) represent the $|\psi|^2$ profiles at five chosen cross-sections (corresponding to five different z including input and output) associated with two beam

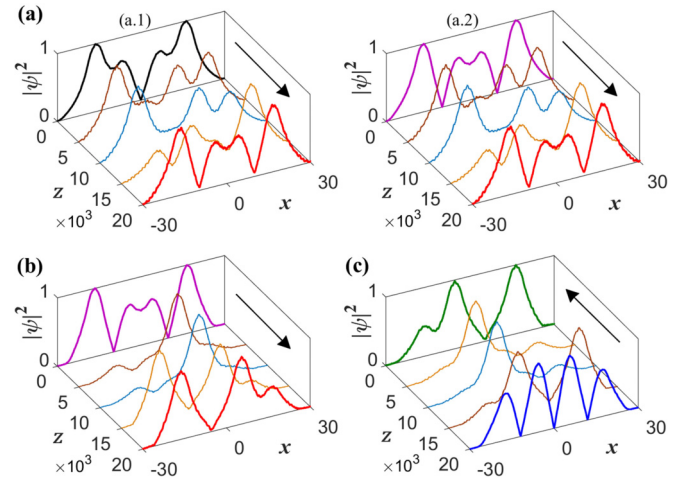


FIG. 7. Normalized field intensities (the profiles of $|\psi|^2$) at different z associated with (a) two beam propagation plots as shown in Fig. 5(a.1) [referred as (a.1) and (a.2)], (b) second beam propagation plot of Fig. 6(a), and (c) third beam propagation plot of Fig. 6(b).

propagation plots shown in Fig. 5(a.1), where the conversions $\psi_1 \rightarrow \psi_2$ (adiabatic) and $\psi_2 \rightarrow \psi_1$ (nonadiabatic) for clockwise dynamical encirclement scheme of only EP2^(1,2) are clearly visible. Figure 7(b) represent similar $|\psi|^2$ -profiles associated with the second beam propagation plot of Fig. 6(a), showing the adiabatic conversion $\psi_2 \rightarrow \psi_1$ during the clockwise dynamical encirclement of both the EP2s, whereas Fig. 7(c) represent the same associated with the third beam propagation plot of Fig. 6(b), showing the adiabatic conversion $\psi_3 \rightarrow \psi_1$ during the anticlockwise dynamical encirclement of both the EP2s. Similar beam evolution plots can be shown for other beam propagation plots.

- [1] T. Kato, *Perturbation Theory for Linear Operators* (Springer, Berlin, 1966).
- [2] N. Moiseyev, *Non-Hermitian Quantum Mechanics* (Cambridge University Press, Cambridge, 2011).
- [3] W. D. Heiss, *Phys. Rev. E* **61**, 929 (2000).
- [4] W. D. Heiss, *J. Phys. A: Math. Theor.* **41**, 244010 (2008).
- [5] W. D. Heiss, *J. Phys. A: Math. Theor.* **45**, 444016 (2012).
- [6] H. Eleuch and I. Rotter, *Phys. Rev. A* **93**, 042116 (2016).
- [7] M. Müller and I. Rotter, *J. Phys. A: Math. Theor.* **41**, 244018 (2008).
- [8] J.-W. Ryu, S.-Y. Lee, and S. W. Kim, *Phys. Rev. A* **85**, 042101 (2012).
- [9] A. Laha, D. Beniwal, and S. Ghosh, *Phys. Rev. A* **103**, 023526 (2021).
- [10] K. Ding, G. Ma, M. Xiao, Z. Q. Zhang, and C. T. Chan, *Phys. Rev. X* **6**, 021007 (2016).
- [11] M.-A. Miri and A. Alù, *Science* **363**, eaar7709 (2019).
- [12] Ş. K. Özdemir, S. Rotter, F. Nori, and L. Yang, *Nature Mater.* **18**, 783 (2019).
- [13] B. Midya, H. Zhao, and L. Feng, *Nature Commun.* **9**, 2674 (2018).
- [14] R. El-Ganainy, K. G. Makris, M. Khajavikhan, Z. H. Musslimani, S. Rotter, and D. N. Christodoulides, *Nature Phys.* **14**, 11 (2018).
- [15] A. A. Mailybaev, O. N. Kirillov, and A. P. Seyranian, *Phys. Rev. A* **72**, 014104 (2005).
- [16] S.-Y. Lee, J.-W. Ryu, S. W. Kim, and Y. Chung, *Phys. Rev. A* **85**, 064103 (2012).
- [17] S. Bhattacharjee, A. Laha, and S. Ghosh, *Phys. Scr.* **94**, 085202 (2019).
- [18] S. Bhattacharjee, H. K. Gandhi, A. Laha, and S. Ghosh, *Phys. Rev. A* **100**, 062124 (2019).
- [19] S. N. Ghosh and Y. D. Chong, *Sci. Rep.* **6**, 19837 (2016).
- [20] J. Doppler, A. A. Mailybaev, J. Böhm, U. Kuhl, A. Girschik, F. Libisch, T. J. Milburn, P. Rabl, N. Moiseyev, and S. Rotter, *Nature (London)* **537**, 76 (2016).
- [21] S. Ke, B. Wang, C. Qin, H. Long, K. Wang, and P. Lu, *J. Lightwave Technol.* **34**, 5258 (2016).
- [22] A. Laha, A. Biswas, and S. Ghosh, *Phys. Rev. Applied* **10**, 054008 (2018).
- [23] X.-L. Zhang, S. Wang, B. Hou, and C. T. Chan, *Phys. Rev. X* **8**, 021066 (2018).

- [24] S. Dey, A. Laha, and S. Ghosh, *Phys. Rev. B* **101**, 125432 (2020).
- [25] X.-L. Zhang and C. T. Chan, *Commun. Phys.* **2**, 63 (2019).
- [26] S. Dey, A. Laha, and S. Ghosh, *J. Opt. Soc. Am. B* **38**, 1297 (2021).
- [27] X. Yin and X. Zhang, *Nature Mater.* **12**, 175 (2013).
- [28] A. Laha, S. Dey, H. K. Gandhi, A. Biswas, and S. Ghosh, *ACS Photonics* **7**, 967 (2020).
- [29] Y. Choi, C. Hahn, J. W. Yoon, S. H. Song, and P. Berini, *Nature Commun.* **8**, 14154 (2017).
- [30] R. Thomas, H. Li, F. M. Ellis, and T. Kottos, *Phys. Rev. A* **94**, 043829 (2016).
- [31] J. Wiersig, *Phys. Rev. A* **93**, 033809 (2016).
- [32] W. Chen, Ş. Kaya Özdemir, G. Zhao, J. Wiersig, and L. Yang, *Nature (London)* **548**, 192 (2017).
- [33] H. Hodaiei, A. U. Hassan, S. Wittek, H. Garcia-Gracia, R. El-Ganainy, D. N. Christodoulides, and M. Khajavikhan, *Nature (London)* **548**, 187 (2017).
- [34] B. Peng, Ş. K. Özdemir, M. Liertzer, W. Chen, J. Kramer, H. Yılmaz, J. Wiersig, S. Rotter, and L. Yang, *Proc. Natl. Acad. Sci. USA* **113**, 6845 (2016).
- [35] H. Hodaiei, A. U. Hassan, W. E. Hayenga, M. A. Miri, D. N. Christodoulides, and M. Khajavikhan, *Opt. Lett.* **41**, 3049 (2016).
- [36] C. Wang, W. R. Sweeney, A. D. Stone, and L. Yang, *Science* **373**, 1261 (2021).
- [37] H. Xu, D. Mason, L. Jiang, and J. G. E. Harris, *Nature (London)* **537**, 80 (2016).
- [38] A. A. Zyablovsky, E. S. Andrianov, and A. A. Pukhov, *Sci. Rep.* **6**, 29709 (2016).
- [39] J. Kullig, C.-H. Yi, M. Hentschel, and J. Wiersig, *New J. Phys.* **20**, 083016 (2018).
- [40] K. Ding, Z. Q. Zhang, and C. T. Chan, *Phys. Rev. B* **92**, 235310 (2015).
- [41] D. A. Bykov and L. L. Doskolovich, *Phys. Rev. A* **97**, 013846 (2018).
- [42] M. Liertzer, L. Ge, A. Cerjan, A. D. Stone, H. E. Türeci, and S. Rotter, *Phys. Rev. Lett.* **108**, 173901 (2012).
- [43] H. Jing, Ş. K. Özdemir, H. Lü, and F. Nori, *Sci. Rep.* **7**, 3386 (2017).
- [44] C. Dembowski, H.-D. Gräf, H. L. Harney, A. Heine, W. D. Heiss, H. Rehfeld, and A. Richter, *Phys. Rev. Lett.* **86**, 787 (2001).
- [45] C. Dembowski, B. Dietz, H.-D. Gräf, H. L. Harney, A. Heine, W. D. Heiss, and A. Richter, *Phys. Rev. Lett.* **90**, 034101 (2003).
- [46] C. Dembowski, B. Dietz, H.-D. Gräf, H. L. Harney, A. Heine, W. D. Heiss, and A. Richter, *Phys. Rev. E* **69**, 056216 (2004).
- [47] H. Menke, M. Klett, H. Cartarius, J. Main, and G. Wunner, *Phys. Rev. A* **93**, 013401 (2016).
- [48] I. Gilary, A. A. Mailybaev, and N. Moiseyev, *Phys. Rev. A* **88**, 010102(R) (2013).
- [49] T. J. Milburn, J. Doppler, C. A. Holmes, S. Portolan, S. Rotter, and P. Rabl, *Phys. Rev. A* **92**, 052124 (2015).
- [50] J. Schnabel, H. Cartarius, J. Main, G. Wunner, and W. D. Heiss, *Phys. Rev. A* **95**, 053868 (2017).